Unveiling a Pump-Induced Magnon Mode via Its Strong Interaction with Walker Modes

J. W. Rao,[1] Bimu Yao,[1,2,*] C. Y. Wang,[1] C. Zhang,[1] Tao Yu,[3,†] and Wei Lu[1,2,‡]

[1]School of Physical Science and Technology, ShanghaiTech University, Shanghai 201210, China

[2]State Key Laboratory of Infrared Physics, Shanghai Institute of Technical Physics, Chinese Academy of Sciences, Shanghai 200083, China

[3]School of Physics, Huazhong University of Science and Technology, Wuhan, 430074, China

(Received 20 April 2022; revised 16 November 2022; accepted 5 January 2023; published 27 January 2023)

We observe a power-dependent anticrossing of Walker spin-wave modes under microwave pumping when a ferrimagnet is placed in a microwave waveguide that does not support any discrete photon mode. We interpret this unexpected anticrossing as the generation of a pump-induced magnon mode that couples strongly to the Walker modes of the ferrimagnet. This anticrossing inherits an excellent tunability from the pump, which allows us to control the anticrossing via the pump power, frequency, and waveform. Further, we realize a remarkable functionality of this anticrossing, namely, a microwave frequency comb, in terms of the nonlinear interaction that mixes the pump and probe frequencies. Such a frequency comb originates from the magnetic dynamics and thereby does not suffer from the charge noise. The unveiled hybrid magnonics driven away from its equilibrium enriches the utilization of anticrossing for coherent information processing.

DOI: 10.1103/PhysRevLett.130.046705

Introduction.—Anticrossing between two coupled bands is a universal phenomenon widely existing in a variety of systems, such as molecules [1–3], hybrid quantum systems [4–7], electric circuits [8], and mechanical devices [9,10]. It leads to the formation of polaritonic quasiparticles, provides the foundation for coherent energy transfer between distinct physical entities [11–16], and has a strong effect on quantum transport. Anticrossing can be produced from either the drive field or the vacuum field. Specifically, driving a Λ-configuration system can lead to the anticrossing with the Autler-Townes (AT) effect [17–19]. Its splitting gap is proportional to the drive field strength and is invaluable for accurate electromagnetic detection. On the other hand, using a cavity to reduce the photon mode volume can greatly enhance the light-matter interaction and thus produce the anticrossing, for instance the anticrossing in cavity magnonics [20–33] caused by the strong photon-magnon coupling. The recent work [34] combines cavity magnonics with Floquet physics and enriches the control of magnon-based anticrossing by taking advantage of nonlinearity and nonequilibrium. However, it relies on coupling magnons to a cavity to constitute the Λ-configuration for AT splitting. It is a basic fact that on replacing the cavity by a waveguide, the discrete photon mode becomes a continuum, and the magnon-based anticrossing vanishes.

In this Letter, however, we observe an anticrossing of Walker modes [35–37] during strong driving of a ferrimagnetic yttrium iron garnet (YIG) sphere on top of a coplanar waveguide (CPW) by microwaves, as illustrated in Fig. 1(a). This waveguide is a broadband microwave device that has no discrete photon modes, and therefore anticrossing is not expected [38,39]. The anticrossing, on the other hand, is not an intrinsic property of the system but is tunable by the pump power P_d with the gap scaling as $P_d^{1/4}$, which makes strong distinction from that of AT

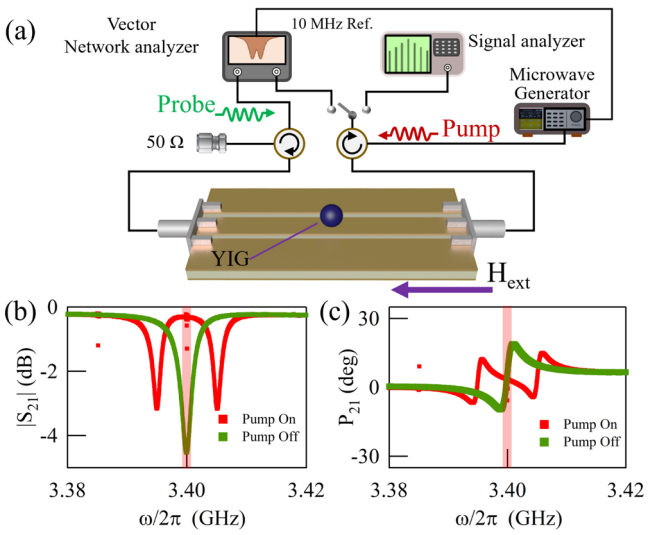

FIG. 1. (a) Experimental configuration. Continuous pump and probe microwaves excite and detect the magnetization dynamics of a YIG sphere placed on top of a CPW. (b),(c) Measured transmission magnitude ($|S_{21}|$) and phase (P_{21}) of the Walker (2,2,0) mode. The red and green squares correspond respectively to the situations with and without the pump (5 dBm). Mode splitting appears after turning on the pump. The scattered data points at 3.384 and 3.4 GHz in both (b) and (c) are spurious signals arising from crosstalk between the pump and probe fields.

 © 2023 American Physical Society

splitting $\propto P_d^{1/2}$. As a phenomenological theory, we interpret the other discrete mode, which couples strongly to the Walker mode to induce the anticrossing, as a pump-induced magnon mode (PIM) [20,40,41]. The PIM can be continuously tuned by the pump up to a saturated frequency, while maintaining a narrow linewidth (~500 kHz). When the anticrossing appears, the radiation of our system reads out multiple peaks with equal frequency intervals, thus demonstrating a frequency comb [42–46] functionality, produced by mixing the pump and probe signals via the nonlinear magnon interaction, including cross-Kerr effect [47–49].

Anticrossing of Walker modes in a waveguide.—The CPW, fabricated on a 22×50 mm^2 RO4350B board, has a standard impedance of 50 Ω. The width of its central strip (1.1 mm) is slightly larger than the diameter of the YIG sphere (1 mm). The gap between the central strip and the two ground planes is 0.24 mm. The YIG sphere placed on top of the central strip of the CPW has a number of spin $N_w \approx 10^{19}$ and saturated magnetization [50] $M = 1.46 \times 10^5$ A/m [Fig. 1(a)]. An external magnetic field H_{ext} is applied to tune the Walker mode frequency ω_w. Two continuous microwaves, namely, the pump and probe, respectively drive and detect the ferromagnetic resonance. The pump, restricted to a single frequency ω_d, has a large power P_d. The probe, produced and received by a vector network analyzer (VNA) for transmission (S_{21}) measurement, has a fixed power of −25 dBm throughout the experiment, but sweeps a wide-band frequency ω_p. A signal analyzer (SA) monitors the radiation spectra of the system, enabling the study of frequency conversion.

Without the pump, we observe several Walker modes of the YIG sphere from the transmission spectrum, as shown in the Supplemental Material [41]. As analytical solutions of the Maxwell and Landau-Lifshitz equations with spherical boundary conditions, Walker modes can be simply viewed as standing spin waves in the YIG sphere [35–37]. Here, we focus on the (2,2,0) Walker mode. Its transmission amplitudes and phases are plotted as green squares in Figs. 1(b) and 1(c), respectively. They can be reproduced well by a standard transmission formula $S_{21} = 1 + \kappa/[i(\omega - \omega_w) - (\kappa + \alpha)]$ with $\omega_w/2\pi = 3.4$ GHz for the Walker mode frequency at 116.5 mT, an external damping rate $\kappa/2\pi = 0.55$ MHz, and an intrinsic damping rate $\alpha/2\pi = 0.85$ MHz.

After we turn on the pump with frequency $\omega_d/2\pi = 3.4$ GHz and power $P_d = 5$ dBm, the former single resonance dramatically splits into two dips with equal intensities, shown by the red squares in Fig. 1(b). The pump-induced splitting (PIS) gap is 10 MHz, much larger than the Walker mode linewidth $(\kappa + \alpha)/2\pi = 1.4$ MHz. At each resonant dip, there exists a phase jump of the microwaves, as shown in Fig. 1(c).

The PIS also exhibits a nontrivial dependence on the external magnetic field H_{ext}. Without the pump, a linear dependence of the Walker mode (ω_w) on H_{ext} is shown in Fig. 2(a), following the Kittel formula [35]. We then turn on the pump and perform the measurement with the same experimental settings. The former linear dispersion is split into two branches with an anticrossing [Fig. 2(b)]. This reveals a strong coupling between the Walker mode and a hidden discrete mode, which oscillates at the pump frequency and is insensitive to any H_{ext}. The two branches follow a dispersion $[\omega_d + \omega_w \pm \sqrt{(\omega_d - \omega_w)^2 + 4g^2}]/2$ with a coupling strength $g/2\pi = 5$ MHz. Their linewidths and amplitudes, extracted from Fig. 2(b), are plotted in Figs. 2(c) and 2(d), respectively. With increasing H_{ext}, the linewidths of the two branches exchange values between 1.4 and 0.55 MHz, while their squared transmission amplitudes exchange values between 0.6 and nearly zero. These features in Figs. 2(b)–2(d) are signatures of a strong coupling effect between two discrete modes. Although the pump-induced mode is invisible in the transmission, the amplitude and linewidth evolution of the anticrossing can help us to reveal its dynamic properties.

The PIS is not restricted to the (2,2,0) mode, but is a general feature of other Walker modes [41]. It cannot be

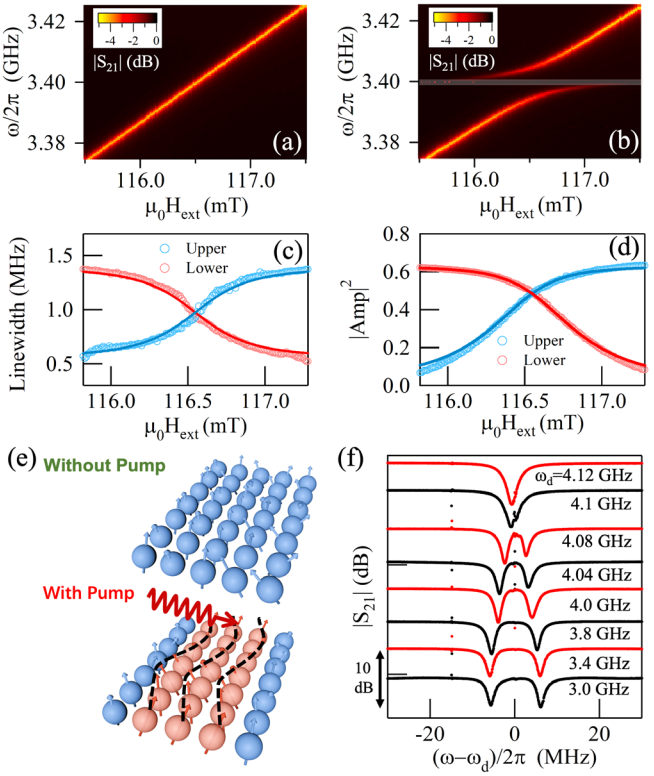

FIG. 2. (a) and (b) Transmission spectra of the Walker mode measured at different H_{ext} without and with the pump. (c) and (d) Linewidths and squared transmission amplitudes of the upper (blue circles) and lower (red circles) branches in (b) as functions of H_{ext}. The solid lines are the results calculated using Eq. (1). (e) The cooperative precession of unsaturated spins under pump as possible origin of PIM. (f) Evolution of PIS when increasing ω_d.

explained by presently known nonlinear mechanisms, including the self-Kerr effect [51,52], the Suhl instability [50,53], and the spin nutation [54]. Moreover, when we replace the CPW with a different microwave device, such as a planar cavity, a microstripline, or a loop antenna, the PIS is still present. Therefore, we exclude the possibility that PIS originates from specific electromagnetic surroundings.

Based on existing knowledge, the known magnon modes in a YIG sphere, including Walker and Damon-Eshbach modes, have no resonance matching the pump frequency that is independent of the magnetic field. We conjecture that, at the low magnetic field, there exist many unsaturated spins in the YIG with random precession. After applying a pump, such unsaturated spins may obtain cooperativity and form a spin wave [Fig. 2(e)]. We formulate a phenomenological model to account for this spin wave, namely, the PIM, but leave the microscopic details to the fitting parameters [41]. To support our assumption, we measure the PIS at different ω_d [Fig. 2(f)]. With increasing ω_d to large H_{ext}, the YIG gradually saturates. The measured PIS closure in Fig. 2(f) indicates the disappearance of PIM. Considering possible disturbance from thermal fluctuations on unsaturated spins, we envision exploring the temperature dependence of PIS, especially at the millikelvin temperatures, can provide more in-depth clues to its microscopic origin.

The PIM's radiation, however, is obscured by the pump, making its direct observation difficult. However, via its interaction with the Walker modes, we can detect it indirectly. We mainly consider the Zeeman interaction between two modes, which is modeled as $F_{\text{in}} = \eta\mu_0\gamma \int_V \mathbf{M}_w(\mathbf{r}) \cdot \mathbf{M}_p(\mathbf{r}) d\mathbf{r}$ [41,52], where η represents an effective demagnetization factor O(1), γ is the electronic gyromagnetic ratio, $\mathbf{M}_w$ and $\mathbf{M}_p$ are the magnetizations of the Walker mode and PIM, respectively, and V is the YIG volume [47]. Note that we have ignored the spin textures of two modes in this effective model, and focus only on the key features of our nontrivial observations.

We denote by $\hat{a}^\dagger(\hat{a})$ and $\hat{b}^\dagger(\hat{b})$, the creation (annihilation) operators of the Walker mode and the PIM, respectively, which couple in the Hamiltonian

$$\begin{aligned}\mathcal{H}/\hbar = {} & \tilde{\omega}_w \hat{a}^\dagger \hat{a} + \tilde{\omega}_d \hat{b}^\dagger \hat{b} + g(\hat{a}^\dagger \hat{b} + \hat{a}\hat{b}^\dagger) + K \hat{a}^\dagger \hat{a} \hat{b}^\dagger \hat{b} \\ & + (\Omega_p \, \hat{a}^\dagger e^{-i\omega_p t} + \text{H.c.}) \\ & + [(\Omega_d \hat{a}^\dagger + \Omega_d' \hat{b}^\dagger) e^{-i\omega_d t} + \text{H.c.}], \end{aligned} \tag{1}$$

where $\tilde{\omega}_w = \omega_w - i(\kappa + \alpha)$ and $\tilde{\omega}_d = \omega_d - i\xi$ are the complex mode frequencies. The PIM's damping rate is $\xi/2\pi = 0.55$ MHz. Ω_p, Ω_d, and Ω_d' correspond to the effective intensities of probe and pump felt by each mode. Two modes' interaction includes (i) a coherent coupling with a strength $g = \eta\mu_0\hbar^2\gamma^3\sqrt{N_w N_p}/\sqrt{2}V$, where N_p represents the PIM's spin number, which should be the magnon number excited by the pump, i.e., $N_p = \langle \hat{b}^\dagger \hat{b} \rangle$, and (ii) a cross-Kerr effect with a coefficient $K = g/\sqrt{N_w N_p}$. Since $N_w, N_p \gg 1$, we have $g \gg K$ [41]. This weak K does not induce obvious frequency shifts for the two hybrid modes, but can lead to frequency conversion, i.e., a portion of system energy is converted to sidebands and generates new magnons. This process is beyond the measurement capability of the VNA, and will be addressed in the frequency comb measurement later.

Driven by the pump, our system mainly oscillates at ω_d. In addition, small fluctuations are induced by the weak probe [41]. Expressing both the steady state and fluctuations in terms of the Walker mode and PIM, we derive the coupling strength [41]

$$g = \sqrt{\sqrt{g_0^2 \kappa A_d^2 - (\xi - \varrho A_d)^2 \Delta^2} - (\xi - \varrho A_d)(\kappa + \alpha)}, \tag{2}$$

where A_d is the pump field amplitude, $\Delta = \omega_w - \omega_d$ is the detuning between two modes, and g_0 and ϱ are two constants [41]. We further linearize the response of the probe and obtain the transmission spectrum

$$S_{21} \approx 1 + \frac{\kappa}{i(\omega_p - \omega_w) - (\kappa + \alpha) + \frac{g^2}{i(\omega_p - \omega_d) - \xi}}, \tag{3}$$

from which the calculated linewidths and amplitudes of the two hybridized modes agree with the experimental findings in Figs. 2(c) and 2(d).

Pump dependence.—We now study the dependence of the anticrossing on the pump frequency ω_d. Figure 3(a) shows the transmission spectra measured at different ω_d but a constant power $P_d = 5$ dBm. With constant H_{ext}, the Walker mode $\omega_w/2\pi$ is fixed at 3.4 GHz, but the PIM can be continuously tuned by varying ω_d. Hence, we tune the PIM to cross the Walker mode and thereby produce an anticrossing [Fig. 3(a)]. The coupling strength at different ω_d are extracted [41] from Fig. 3(a) and plotted as blue circles in Fig. 3(b). It varies slowly near resonance, but drops quickly at large detuning. This variation is well reproduced by Eq. (2), shown as the red line in Fig. 3(b).

We then address the power dependence of the anticrossing, which shows that this effect is not an intrinsic property like the cavity magnon polariton [20–33], but an effect induced by the pump. To this end, we set $\omega_d/2\pi =$ 3.4 GHz and vary P_d from −30 to 20 dBm. With a low power (−30 dBm) we only observe a single dip, which splits into a doublet at the power around −20 dBm, as shown in Fig. 3(c). As P_d increases further, the splitting gap increases significantly. Figure 3(d) shows the coupling strength g, extracted from each spectrum, as a function of P_d. Through fitting we find the scaling relation $g/2\pi = C \cdot P_d^{1/4}$, with just one fitting parameter $C = 3.7\,\text{MHz}/\sqrt[4]{\text{mW}}$. This relation is again reproduced by Eq. (2), since $A_d \propto \sqrt{P_d}$.

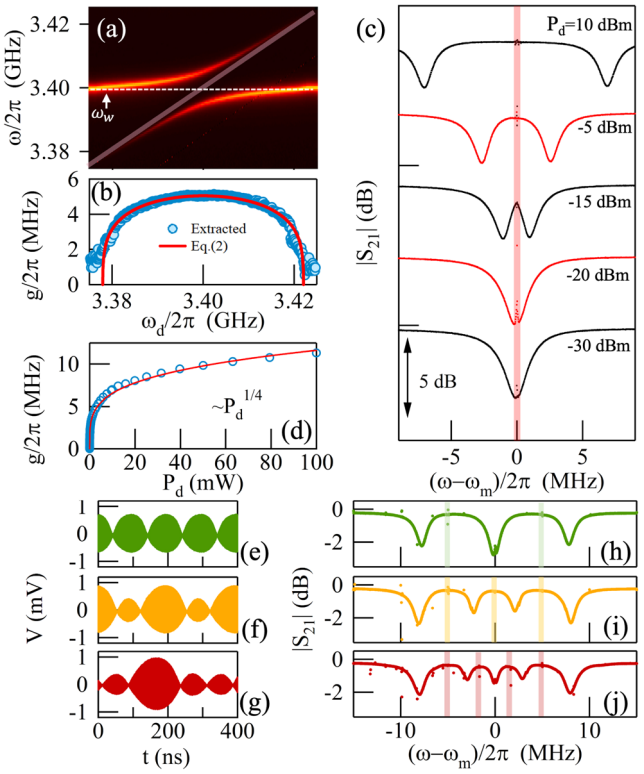

FIG. 3. (a) and (b) Measured PIS transmission and extracted coupling strength g as function of ω_d. The red line is calculated by using Eq. (2). (c) Power dependence of the PIS. The pump is indicated by the pink strips in (a) and (c). (d) Coupling strength g as a function of P_d, which is well fitted by $g \propto P_d^{1/4}$ by the red line. (e)–(g) Synthetic pumps with time-dependent amplitudes, consisting of $N = 2$, 3, or 4 main tones with equal intensities, constant phases, and equal frequency intervals represented by the colored strips in (h)–(j), where three, four, and five hybridized magnon modes appear.

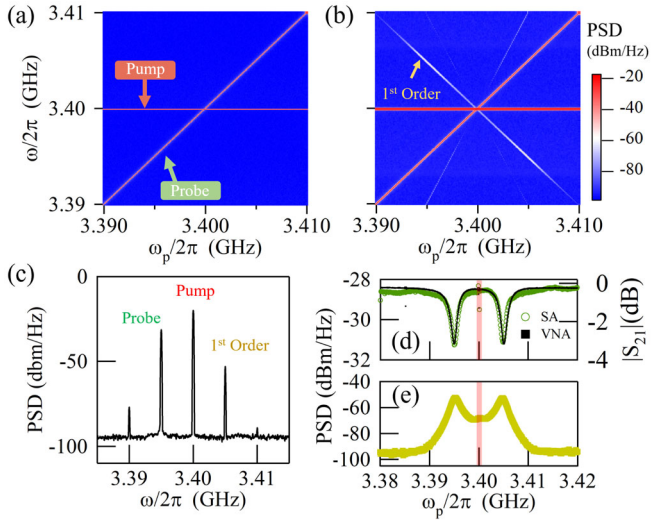

FIG. 4. (a) and (b) Measured radiation spectra at $H_{\text{ext}} = 0$ and $\omega_w/2\pi = 3.4$ GHz under $\omega_d/2\pi = 3.4$ GHz. The probe frequency ω_p is varied from 3.39 to 3.41 GHz. (c) Frequency comb measured at $\omega_p/2\pi = 3.395$ GHz. (d) Amplitude of the probe extracted from (b) (green circles) as a function of ω_p. Two hybridized magnon modes are consistent with the VNA measurement (black squares). (e) Amplitude of the first-order sideband signal as a function of ω_p, which reaches the maximum at two hybridized modes.

The PIM-Walker mode coupling can also be controlled by modulating the pump waveform. We replace the single-frequency pump with synthetic pumps consisting of $N = 2$, 3, or 4 main tones with equal intensities, constant phases, and equal frequency intervals. Their amplitudes are time dependent, as shown in Figs. 3(e)–3(g). The corresponding main tones are indicated by the vertical strips in Figs. 3(h)–3(j). Each tone generates a PIM, which then couples with the Walker mode, resulting in $N + 1$ hybridized modes. This approach of generating multiple hybridized magnon modes relies simply on the waveform manipulation, which thus may find applications in magnon-based coherent information storage [55] or Floquet electromagnonics [34].

Frequency comb.—Besides the linear coupling, the nonlinear PIM-Walker mode interaction enables frequency conversion. We set the pump as $\omega_d/2\pi = 3.4$ GHz and $P_d = 5$ dBm. The probe frequency ω_p is swept from 3.39 to 3.41 GHz successively. At each ω_p, the radiation spectrum of our system, i.e., the power spectral density (PSD), is recorded by the SA. Figure 4(a) shows the measured results at zero H_{ext}, i.e., $\omega_w = 0$. Two signals simply cross each other, and no sidebands appear. We then tune the Walker mode to match the pump frequency, i.e., $\omega_w/2\pi = \omega_d/2\pi = 3.4$ GHz, and keep all other settings unchanged. From the measured PSD [Fig. 4(b)], we observe a frequency comb. Beside the pump and probe, the first-, second- and third-order sideband signals occur at $(2\omega_d - \omega_p)/2\pi$, $(2\omega_p - \omega_d)/2\pi$, and $(3\omega_d - 2\omega_p)/2\pi$, respectively. Figure 4(c) shows a spectrum measured at $\omega_p/2\pi = 3.395$ GHz. The sideband signals are several orders of magnitude weaker than the detected pump and probe.

The amplitudes of all the comb teeth change with the probe frequency ω_p. Here we extract the amplitudes of the probe and the first-order sideband signal from Fig. 4(b) and plot them in Figs. 4(d) and 4(e). From the probe [green dots in Fig. 4(d)], we see two hybridized modes at 3.395 GHz and 3.405 GHz, consistent with the transmission measurement (black line). These two modes are two absorption channels for the probe, at which the energy absorption and conversion is most efficient. Consequently, the first-order sideband signal reaches its maximum [Fig. 4(e)]. Based on the Hamiltonian [Eq. (1)], we numerically simulate the frequency comb arising from the nonlinear magnon interaction, including the cross-Kerr effect, which reproduces our experimental observations well [41].

Conclusion and discussion.—We have observed an anticrossing of Walker modes, when a YIG sphere is

driven by microwaves in a waveguide. This phenomenon resembles a transcritical bifurcation in nonlinear physics [56], but has a different physical origin. If we assume that a driven magnon mode, i.e., the PIM, is induced by the pump, we can naturally reproduce the key features of our observations. The PIM is not directly observed with the pump-probe technique, but is traced via its interactions with the Walker modes.

Our study demonstrates that a magnet driven away from equilibrium can exhibit interesting and potentially useful properties [57]. The pump-induced anticrossing in our Letter has a cooperativity higher than 120, unambiguously demonstrating the strong coupling effect. This anticrossing exhibits flexible controllability by the pump frequency, power, and waveform. Such an excellent flexibility is rarely achievable with cavity magnon polaritons. Although performing below a saturated frequency, the PIM operates robustly in the *S* band that is vital to wireless networking [58] and quantum information processing [59].

The PIM also enables the mixing of the pump and probe and hence generates a frequency comb. This frequency comb is constructed purely on the basis of magnetic nonlinearity and hence does not suffer from the charge noise from electric nonlinearities [8]. Utilizing our frequency comb, we may be able to realize coherent information conversion with ultralow noise or study spin-wave solitons in magnonics. After lifting a corner of the veil covering the PIM, we will further investigate more of the nature and functionality of this nonequilibrium mode.

This work has been funded by the National Natural Science Foundation of China under Grants No. 11974369, No. 12122413, No. 12204306, No. 0214012051, and No. 11991063; STCSM No. 21JC1406200 and No. 22JC1403300; the Youth Innovation Promotion Association No. 2020247; Strategic priority research No. XDB43010200 of CAS; the SITP Independent Foundation; the Shanghai Pujiang Program (No. 22PJ1410700); the National Key R&D Program of China (No. 2022YFA1404603); and the startup grant of Huazhong University of Science and Technology (Grants No. 3004012185 and No. 3004012198).

*yaobimu@mail.sitp.ac.cn
†taoyuphy@hust.edu.cn
‡luwei@mail.sitp.ac.cn

[1] D. G. Lidzey, D. Bradley, M. Skolnick, T. Virgili, S. Walker, and D. Whittaker, Strong exciton–photon coupling in an organic semiconductor microcavity, Nature (London) **395**, 53 (1998).
[2] W. L. Meerts and I. Ozier, Avoided-crossing molecular-beam experiments on fluoroform (CF_3H) and fluoroform-d (CF_3D), J. Chem. Phys. **75**, 596 (1981).
[3] L. Benthem, J. H. Lichtenbelt, and D. A. Wiersma, Study of the residual linewidth of the level-anti-crossing signal in p-benzoquinone, Chem. Phys. **29**, 367 (1978).
[4] A. Bylinkin, M. Schnell, F. Calavalle, P. Li, J. Taboada-Gutièrrez, S. Liu, J. H. Edgar, F. Casanova, L. E. Hueso, P. Alonso-Gonzalez *et al.*, Real-space observation of vibrational strong coupling between propagating phonon polaritons and organic molecules, Nat. Photonics **15**, 197 (2021).
[5] D. Lachance-Quirion, S. P. Wolski, Y. Tabuchi, S. Kono, K. Usami, and Y. Nakamura, Entanglement-based single-shot detection of a single magnon with a superconducting qubit, Science **367**, 425 (2020).
[6] L. Fan, C.-L. Zou, R. Cheng, X. Guo, X. Han, Z. Gong, S. Wang, and H. X. Tang, Superconducting cavity electro-optics: A platform for coherent photon conversion between superconducting and photonic circuits, Sci. Adv. **4**, eaar4994 (2018).
[7] T. S. Koh, J. K. Gamble, M. Friesen, M. Eriksson, and S. Coppersmith, Pulse-Gated Quantum-Dot Hybrid Qubit, Phys. Rev. Lett. **109**, 250503 (2012).
[8] D. M. Pozar, *Microwave Engineering* (John Wiley & Sons, New York, 2011).
[9] E. Verhagen, S. Deléglise, S. Weis, A. Schliesser, and T. J. Kippenberg, Quantum-coherent coupling of a mechanical oscillator to an optical cavity mode, Nature (London) **482**, 63 (2012).
[10] A. B. Pippard, *The Physics of Vibration* (Cambridge University Press, Cambridge, England, 2007).
[11] K. Huang, Lattice vibrations and optical waves in ionic crystals, Nature (London) **167**, 779 (1951).
[12] H. Deng, H. Haug, and Y. Yamamoto, Exciton-polariton Bose-Einstein condensation, Rev. Mod. Phys. **82**, 1489 (2010).
[13] T. Byrnes, N. Y. Kim, and Y. Yamamoto, Exciton–polariton condensates, Nat. Phys. **10**, 803 (2014).
[14] K. Shen and G. E. Bauer, Laser-Induced Spatiotemporal Dynamics of Magnetic Films, Phys. Rev. Lett. **115**, 197201 (2015).
[15] A. Kamra, H. Keshtgar, P. Yan, and G. E. Bauer, Coherent elastic excitation of spin waves, Phys. Rev. B **91**, 104409 (2015).
[16] H. Hayashi and K. Ando, Spin Pumping Driven by Magnon Polarons, Phys. Rev. Lett. **121**, 237202 (2018).
[17] S. H. Autler and C. H. Townes, Stark effect in rapidly varying fields, Phys. Rev. **100**, 703 (1955).
[18] M. A. Sillanpää, J. Li, K. Cicak, F. Altomare, J. I. Park, R. W. Simmonds, G.-S. Paraoanu, and P. J. Hakonen, Autler-Townes Effect in a Superconducting Three-Level System, Phys. Rev. Lett. **103**, 193601 (2009).
[19] E. Saglamyurek, T. Hrushevskyi, A. Rastogi, K. Heshami, and L. J. LeBlanc, Coherent storage and manipulation of broadband photons via dynamically controlled Autler–Townes splitting, Nat. Photonics **12**, 774 (2018).
[20] B. Z. Rameshti, S. V. Kusminskiy, J. A. Haigh, K. Usami, D. Lachance-Quirion, Y. Nakamura, C.-M. Hu, H. X. Tang, G. E. Bauer, and Y. M. Blanter, Cavity magnonics, Phys. Rep. **979**, 1 (2022).

[21] Ö. O. Soykal and M. Flatté, Strong Field Interactions between a Nanomagnet and a Photonic Cavity, Phys. Rev. Lett. **104**, 077202 (2010).
[22] H. Huebl, C. W. Zollitsch, J. Lotze, F. Hocke, M. Greifenstein, A. Marx, R. Gross, and S. T. Goennenwein, High Cooperativity in Coupled Microwave Resonator Ferrimagnetic Insulator Hybrids, Phys. Rev. Lett. **111**, 127003 (2013).
[23] Y. Tabuchi, S. Ishino, A. Noguchi, T. Ishikawa, R. Yamazaki, K. Usami, and Y. Nakamura, Coherent coupling between a ferromagnetic magnon and a superconducting qubit, Science **349**, 405 (2015).
[24] L. Bai, M. Harder, P. Hyde, Z. Zhang, C.-M. Hu, Y. Chen, and J. Q. Xiao, Cavity Mediated Manipulation of Distant Spin Currents Using a Cavity-Magnon-Polariton, Phys. Rev. Lett. **118**, 217201 (2017).
[25] M. Goryachev, W. G. Farr, D. L. Creedon, Y. Fan, M. Kostylev, and M. E. Tobar, High-Cooperativity Cavity QED with Magnons at Microwave Frequencies, Phys. Rev. Appl. **2**, 054002 (2014).
[26] D. Lachance-Quirion, Y. Tabuchi, A. Gloppe, K. Usami, and Y. Nakamura, Hybrid quantum systems based on magnonics, Appl. Phys. Express **12**, 070101 (2019).
[27] B. Bhoi and S.-K. Kim, Roadmap for photon-magnon coupling and its applications, in *Solid State Physics* (Elsevier, New York, 2020), Vol. 71, pp. 39–71.
[28] Y. Cao, P. Yan, H. Huebl, S. T. B. Goennenwein, and G. E. W. Bauer, Exchange magnon-polaritons in microwave cavities, Phys. Rev. B **91**, 094423 (2015).
[29] I. Boventer, M. Pfirrmann, J. Krause, Y. Schön, M. Kläui, and M. Weides, Complex temperature dependence of coupling and dissipation of cavity magnon polaritons from millikelvin to room temperature, Phys. Rev. B **97**, 184420 (2018).
[30] W. Yu, J. Wang, H. Yuan, and J. Xiao, Prediction of Attractive Level Crossing via a Dissipative Mode, Phys. Rev. Lett. **123**, 227201 (2019).
[31] V. L. Grigoryan, K. Shen, and K. Xia, Synchronized spin-photon coupling in a microwave cavity, Phys. Rev. B **98**, 024406 (2018).
[32] J. Rao, P. Xu, Y. Gui, Y. Wang, Y. Yang, B. Yao, J. Dietrich, G. Bridges, X. Fan, D. Xue *et al.*, Interferometric control of magnon-induced nearly perfect absorption in cavity magnonics, Nat. Commun. **12**, 1 (2021).
[33] Y. Li, V. G. Yefremenko, M. Lisovenko, C. Trevillian, T. Polakovic, T. W. Cecil, P. S. Barry, J. Pearson, R. Divan, and V. Tyberkevych, Coherent Coupling of Two Remote Magnonic Resonators Mediated by Superconducting Circuits, Phys. Rev. Lett. **128**, 047701 (2022).
[34] J. Xu, C. Zhong, X. Han, D. Jin, L. Jiang, and X. Zhang, Floquet Cavity Electromagnonics, Phys. Rev. Lett. **125**, 237201 (2020).
[35] L. R. Walker, Magnetostatic modes in ferromagnetic resonance, Phys. Rev. **105**, 390 (1957).
[36] J. Dillon Jr, Ferrimagnetic resonance in yttrium iron garnet, Phys. Rev. **105**, 759 (1957).
[37] A. Gloppe, R. Hisatomi, Y. Nakata, Y. Nakamura, and K. Usami, Resonant Magnetic Induction Tomography of a Magnetized Sphere, Phys. Rev. Appl. **12**, 014061 (2019).
[38] T. Yu, X. Zhang, S. Sharma, Y. M. Blanter, and G. E. Bauer, Chiral coupling of magnons in waveguides, Phys. Rev. B **101**, 094414 (2020).
[39] T. Yu, Y.-X. Zhang, S. Sharma, X. Zhang, Y. M. Blanter, and G. E. Bauer, Magnon Accumulation in Chirally Coupled Magnets, Phys. Rev. Lett. **124**, 107202 (2020).
[40] P. H. Bryant, C. D. Jeffries, and K. Nakamura, Spin-wave dynamics in a ferrimagnetic sphere, Phys. Rev. A **38**, 4223 (1988).
[41] See Supplementary Material at http://link.aps.org/supplemental/10.1103/PhysRevLett.130.046705 for additional information of the Hamiltonian of the coupled PIM-Walker mode, the experimental results of the strong PIM-Walker modes coupling and the numerical simulation, which includes Refs. [35,37,40].
[42] Z. Wang, H. Yuan, Y. Cao, Z.-X. Li, R. A. Duine, and P. Yan, Magnonic Frequency Comb through Nonlinear Magnon-Skyrmion Scattering, Phys. Rev. Lett. **127**, 037202 (2021).
[43] T. Hula, K. Schultheiss, F. J. T. Goncalves, L. Körber, M. Bejarano, M. Copus, L. Flacke, L. Liensberger, A. Buzdakov, A. Kákay *et al.*, Spin-wave frequency combs, Appl. Phys. Lett. **121**, 112404 (2022).
[44] A. Schliesser, N. Picqué, and T. W. Hänsch, Mid-infrared frequency combs, Nat. Photonics **6**, 440 (2012).
[45] T. J. Kippenberg, R. Holzwarth, and S. A. Diddams, Microresonator-based optical frequency combs, Science **332**, 555 (2011).
[46] I. Coddington, W. C. Swann, and N. R. Newbury, Coherent Multiheterodyne Spectroscopy Using Stabilized Optical Frequency Combs, Phys. Rev. Lett. **100**, 013902 (2008).
[47] W.-J. Wu, D. Xu, J. Qian, J. Li, Y.-P. Wang, and J. You, Observation of magnon cross-Kerr effect in cavity magnonics, arXiv:2112.13807.
[48] I.-C. Hoi, A. F. Kockum, T. Palomaki, T. M. Stace, B. Fan, L. Tornberg, S. R. Sathyamoorthy, G. Johansson, P. Delsing, and C. Wilson, Giant Cross–Kerr Effect for Propagating Microwaves Induced by an Artificial Atom, Phys. Rev. Lett. **111**, 053601 (2013).
[49] Y.-B. Sheng, F.-G. Deng, and H.-Y. Zhou, Efficient polarization-entanglement purification based on parametric down-conversion sources with cross-Kerr nonlinearity, Phys. Rev. A **77**, 042308 (2008).
[50] M. Elyasi, Y. M. Blanter, and G. E. Bauer, Resources of nonlinear cavity magnonics for quantum information, Phys. Rev. B **101**, 054402 (2020).
[51] Y.-P. Wang, G.-Q. Zhang, D. Zhang, T.-F. Li, C.-M. Hu, and J. You, Bistability of Cavity Magnon Polaritons, Phys. Rev. Lett. **120**, 057202 (2018).
[52] G. Zhang, Y. Wang, and J. You, Theory of the magnon Kerr effect in cavity magnonics, Sci. China Phys. Mech. Astron. **62**, 1 (2019).
[53] P. Anderson and H. Suhl, Instability in the motion of ferromagnets at high microwave power levels, Phys. Rev. **100**, 1788 (1955).
[54] Y. Li, V. V. Naletov, O. Klein, J. L. Prieto, M. Muñoz, V. Cros, P. Bortolotti, A. Anane, C. Serpico, and G. de Loubens, Nutation Spectroscopy of a Nanomagnet Driven into Deeply Nonlinear Ferromagnetic Resonance, Phys. Rev. X **9**, 041036 (2019).

[55] X. Zhang, C.-L. Zou, N. Zhu, F. Marquardt, L. Jiang, and H. X. Tang, Magnon dark modes and gradient memory, Nat. Commun. **6**, 1 (2015).

[56] J. D. Crawford, Introduction to bifurcation theory, Rev. Mod. Phys. **63**, 991 (1991).

[57] A. de la Torre, D. M. Kennes, M. Claassen, S. Gerber, J. W. McIver, and M. A. Sentef, Colloquium: Nonthermal pathways to ultrafast control in quantum materials, Rev. Mod. Phys. **93**, 041002 (2021).

[58] R. Sharma, R. Mishra, T. Ngo, Y.-X. Guo, S. Fukami, H. Sato, H. Ohno, and H. Yang, Electrically connected spin-torque oscillators array for 2.4 GHz wifi band transmission and energy harvesting, Nat. Commun. **12**, 1 (2021).

[59] R. Amsüss, C. Koller, T. Nöbauer, S. Putz, S. Rotter, K. Sandner, S. Schneider, M. Schramböck, G. Steinhauser, H. Ritsch *et al.*, Cavity QED with Magnetically Coupled Collective Spin States, Phys. Rev. Lett. **107**, 060502 (2011).